Preliminary assessment of ship detection and trajectory evaluation using distributed acoustic sensing on an optical fiber telecom cable

Diane Rivet, Benoit de Cacqueray, Anthony Sladen, Aurélien Roques, and Gaëtan Calbris

Citation: The Journal of the Acoustical Society of America **149**, 2615 (2021); doi: 10.1121/10.0004129
View online: https://doi.org/10.1121/10.0004129
View Table of Contents: https://asa.scitation.org/toc/jas/149/4
Published by the Acoustical Society of America

JASA ARTICLE

Preliminary assessment of ship detection and trajectory evaluation using distributed acoustic sensing on an optical fiber telecom cable

Diane Rivet,[1,a)] Benoit de Cacqueray,[2] Anthony Sladen,[1] Aurélien Roques,[3] and Gaëtan Calbris[4]

[1]Université de la Côte d'Azur, Observatoire de la Côte d'Azur, CNRS, IRD, Géoazur, 250 Route d'Albert Einstein, 06220 Valbonne, France

[2]Thales Defense Mission System, 525 Route des Dolines, 06560 Valbonne, France

[3]Lycée Jules Ferry, 06400 Cannes, France

[4]FEBUS-Optics, Technopole Helioparc, 2 Avenue Président Pierre Angot, 64 000 Pau, France

ABSTRACT:

Distributed acoustic sensing (DAS) is a recent instrumental approach allowing the conversion of fiber-optic cables into dense arrays of acoustic sensors. This technology is attractive in marine environments where instrumentation is difficult to implement. A promising application is the monitoring of environmental and anthropic noise, leveraging existing telecommunication cables on the seafloor. We assess the ability of DAS to monitor such noise using a 41.5 km-long cable offshore of Toulon, France, focusing on a known and localized source. We analyze the noise emitted by the same tanker cruising above the cable, first 5.8 km offshore in 85 m deep bathymetry, and then 20 km offshore, where the seafloor is at a depth of 2000 m. The spectral analysis, the Doppler shift, and the apparent velocity of the acoustic waves striking the fiber allow us to separate the ship radiated noise from other noise. At 85 m water depth, the signal-to-noise ratio is high, and the trajectory of the boat is recovered with beamforming analysis. At 2000 m water depth, although the acoustic signal of the ship is more attenuated, signals below 50 Hz are detected. These results confirm the potential of DAS applied to seafloor cables for remote monitoring of acoustic noise even at intermediate depth. https://doi.org/10.1121/10.0004129

(Received 19 June 2020; revised 11 March 2021; accepted 15 March 2021; published online 14 April 2021)

[Editor: James F. Lynch] Pages: 2615–2627

I. INTRODUCTION

Ambient noise in the ocean results from natural and anthropogenic sources. The anthropogenic noise produced by maritime traffic has increased dramatically with the development of industrialization and global trading (Frisk, 2012). Over the last decade, the scientific community has shown that it strongly impacts all of marine fauna, from mammals to zooplankton, including fish, sea turtles, and invertebrates (e.g., Williams *et al.*, 2015; Mustonen *et al.*, 2020). For example, marine mammals use sound for vital activities such as finding food, detecting predators, breeding, and navigation. There is now a strong awareness in the community of a need to limit man-made underwater noise, and international efforts have led to legislation at regional and international levels to limit the impact on marine ecosystems (Merchant, 2019).

Maritime traffic also encompasses important safety and security aspects of high priority for international institutions. Indeed, maritime surveillance is crucial for key infrastructure such as harbors and power plants. Also, submarine telecom cables are critical infrastructures for global communications that are frequently damaged by anchors, seabed trawlers, and other types of activities (Rønnekleiv *et al.*, 2019).

Automatic identification system (AIS) data provide unique identification, position, and trajectories of vessels. From the type, size, and speed of the ship reported in AIS, the radiated noise source level can be compared with measurements (Wales and Heitmeyer, 2011; McKenna *et al.*, 2012) or predicted using shipping noise models (e.g., Wales and Heitmeyer, 2002), but oceanographic conditions, as well as ship design, can strongly modify the radiated noise (e.g., McKenna *et al.*, 2013). Furthermore, AIS is self-declarative and only involves large vessels (Vespe *et al.*, 2012). Yet in coastal areas, small vessels without AIS, such as recreational ships, can generate significantly more noise than AIS vessels (Hermannsen *et al.*, 2019). Therefore, to better and independently survey maritime traffic and evaluate the impact of anthropogenic noise source on marine species, continuous monitoring of acoustic noise needs to be done both on the coast and offshore.

Passive acoustic instruments developed to study anthropic and natural underwater noise, such as high-frequency acoustic recording packages (HARPs), can be deployed from boats anywhere (Wiggins and Hildebrand, 2007). This instrumentation provides broadband 10 Hz to

[a)]Electronic mail: diane.rivet@geoazur.unice.fr, ORCID: 0000-0003-4697-4460.

160 kHz omnidirectional acoustic measurements for an extended period of time (up to 300 days). Ocean bottom seismometers (OBS) often include a hydrophone and can provide low frequency (<400 Hz) acoustical records up to 4 yrs using long-term autonomous platforms such as MUG-OBS (Hello *et al.*, 2019). However, though these acoustic instruments can be deployed anywhere, they do not allow data to be transmitted in real time. Other solutions outside academia like SOSUS (Sound Surveillance System) with horizontal arrays moored on the seafloor can provide real-time sound measurements but with very restricted access to scientists (Nishimura and Conlon, 1994). Overall, measuring acoustic noise over long distances continuously and for an extended period of time with conventional passive acoustic instruments requires expensive installation and maintenance.

Distributed acoustic sensing (DAS) on existing seafloor optical cables provides remote monitoring of the acoustic noise over several tens of kilometers offshore at relatively low cost, but the feasibility of monitoring acoustic waves in all oceanic domains and bandwidths remains to be assessed. Measuring acoustic noise over several tens of kilometers from the shore enables real-time monitoring. However, DAS delivers huge data volumes (a terabyte per day), and relevant on-the-fly processing to ensure real-time monitoring of acoustic noise is not yet available.

DAS measures both elastic and acoustic waves striking optical fibers. This technology has the potential to strongly impact many scientific domains, and in recent years, there has been a growing interest in applications in the earth and environmental sciences. DAS exploits changes in the light that is backscattered from random nano defects in the optical fiber to sense passing acoustic or seismic waves. These external mechanical waves induce a longitudinal strain of the fiber, which can be related to a linear phase shift of the Rayleigh backscattered light. The strain or strain-rate is measured from the phase changes over a distance called the gauge length and thus corresponds to the integration of the strain or strain-rate along the gauge length. Figure 1 describes the principle of DAS acquisition and instrumental setup, and in Appendix A, we express the strain and strain-rate measured by DAS for acoustic waves striking the fiber. In seismology, seismic waves are generally measured with a gauge length of about 10 m (e.g., Jousset *et al.*, 2018, Ajo-Franklin *et al.*, 2019).

DAS has proved to be efficient for monitoring sensitive infrastructures such as pipelines, railways, and dams and is becoming more and more common in seismic imaging and in the monitoring of oil fields and wells (e.g., Mateeva *et al.*, 2013; Miller *et al.*, 2016; Lellouch *et al.*, 2019). Terrestrial seismology applications use either dedicated optical fiber cables dug in the soil (e.g., Daley *et al.*, 2013; Feigl and Parker, 2019) or telecom dark fiber (e.g., Dou *et al.*, 2017; Yu *et al.*, 2019). Academic DAS applications in the underwater environment started in 2019 (Sladen *et al.*, 2019; Lindsey *et al.*, 2019; Williams *et al.*, 2019) with numerous observations—small local seismicity, large teleseismic earthquakes, surface gravity waves, microseismic noise—all with unprecedented spatial resolution. However, these studies focused on the low-frequency content of the DAS measurements, and the true potential of the approach at higher frequency than those used in seismology ($f > 20$ Hz) still needs to be explored and quantified. Under shallow water depth conditions (30 m), Rønnekleiv *et al.* (2019) demonstrated the potential of DAS to detect and distinguish boats and trawlers. The drawbacks of DAS versus hydrophones are related to a more limited bandwidth at high frequency (the acquisition rate is controlled by the length of the fiber—the light pulse has to travel back and forth before the next pulse is emitted) and a cosine square angular sensitivity that renders DAS blind to signals arriving from a direction closely perpendicular to that of the optical fiber cable (Mateeva *et al.*, 2014). Some progress has been made to counteract this last point through helically wound fibers that recover energy from all directions (e.g., Hornman, 2017; Kuvshinov, 2016). However, these limitations are in some way mitigated by the dense sampling in space of the waves hitting the fiber. This high resolution in space leads to an improvement in the signal-to-noise ratio (SNR) by simple summation of the strain-rate observations and in the recovery of the azimuth and position of the acoustic sources through beamforming. Here, we further explore the potential of the technology to monitor and recognize anthropic acoustic noise sources using a well-identified and localized source of acoustic noise in both shallow and deep water.

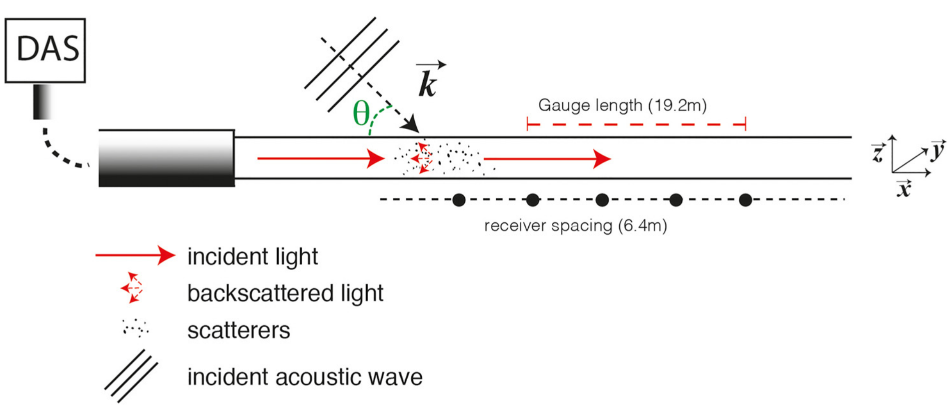

FIG. 1. (Color online) DAS acquisition principle and spatial sensing setup. The DAS acquisition unit is sending a light pulse inside a dark optical fiber. Along the path, the laser pulse interacts with the molecular-scale random scatters inherently present in all telecom fibers. The phase of the refracted light is analyzed for a set of virtual receivers regularly spaced, here 6.4 m. The phase difference is analyzed over a gauge length of 19.2 m to derive the strain-rate variations over that segment.

https://doi.org/10.1121/10.0004129

II. METHOD AND INSTRUMENTAL SETUP

The DAS acquisitions were made on a 41.5 km-long electro-optic telecommunication cable from Alcatel deployed offshore of Toulon in the south of France. The MEUST–NUMerEnv project (Mediterranean Eurocentre for Underwater Sciences and Technologies–Neutrino Mer Environnement; Lamare, 2016) is operating the cable and provides power and data transmission for numerous oceanographic studies in the framework of the EMSO program (European Multidisciplinary Seafloor Observatory; Favali and Beranzoli, 2009) and for the KM3NeT/ORCA (Oscillation Research with Cosmics in the Abyss) neutrino detector (Coyle, 2017). Crossing different oceanic domains of the Mediterranean margin, from the continental shelf to the abyssal plain, the cable, which is simply resting on the seafloor, reaches a depth of 2400 m on the abyssal plain (Fig. 2). From 2.1 km up to 17.2 km off the coast, the cable armoring is single armoring heavy (SAH) and then lightweight protection (LWP) for the remaining 24 km.

The DAS interrogator, provided by Febus Optics (Pau, France), was used from February 19 to 24, 2018. In this experiment, the gauge length was fixed to 19.2 m with a spatial sampling of 6.4 m (Fig. 1).

With a temporal sampling of 2 kHz, waves up to 1 kHz can be accurately retrieved with no temporal aliasing. With this configuration, DAS covers the low frequency range of hydrophones. When processing DAS as an array of receivers using beamforming and frequency-wavenumber (*f-k*) representation, we should also consider the maximum frequency for non-spatially aliased signals. The Nyquist frequency f_N is related to the apparent wave velocity and the spatial sampling Δx through the relation $f_N = c/(2\cos(\theta)\Delta x)$ with c the velocity and θ the bearing angle. For acoustic waves traveling parallel to the fiber cable (for a bearing of 0° or 180°) and having a velocity in seawater of 1500 m/s, the spatial sampling allows the recording of non-spatially aliased acoustic signals up to 117 Hz. Above this frequency, false sources can appear in beamform analysis.

Large vessels report their position to the AIS database. This allowed us to identify that during the DAS acquisition, an 85 m long tanker passed twice over the fiber-optic cable, first 5.8 km offshore with a N 260° route at a velocity of 11 knots, and a few days later, the same tanker passed over the cable at 20 km from the coast with a N 83° route at a velocity of 7.8 knots, crossing the fiber at an angle of 71° (Fig. 2, red bars).

III. MARITIME VESSEL NOISE DETECTION

There is already a long history of studies modeling radiated ship noise (e.g., Gray and Greeley, 1980). The variety of potential noise sources and their interactions makes the topic complex to summarize (Fournier, 2009). However, a constant feature of ship radiated noise is a spectrum characterized by two main components (e.g., Pillon, 2016). The first one is a signal resulting from multiple sources like cavitation, pumps, fans, and fluid flowing in the pipes or along the shell. This component is sometimes considered as having a Gaussian shape with a maximum at a few dozens of Hertz. The second component is a sum of narrowband signals coming from rotating elements (mainly, but not only, linked to propeller activity) and electrical wires (50 or 60 Hz). Frequencies higher than 1 kHz are also characterized by narrowband signals, often with a noise floor showing a decreasing slope of several dB per decade.

At 85 m depth, strain-rate records on the fiber show both features of ship radiated noise: the Fourier transform of 8 min of signals coming from one DAS receiver shows high amplitude narrowband signals (Fig. 3). The intensity recorded by the DAS system in this experiment is uncalibrated; therefore, we express the power relative to the

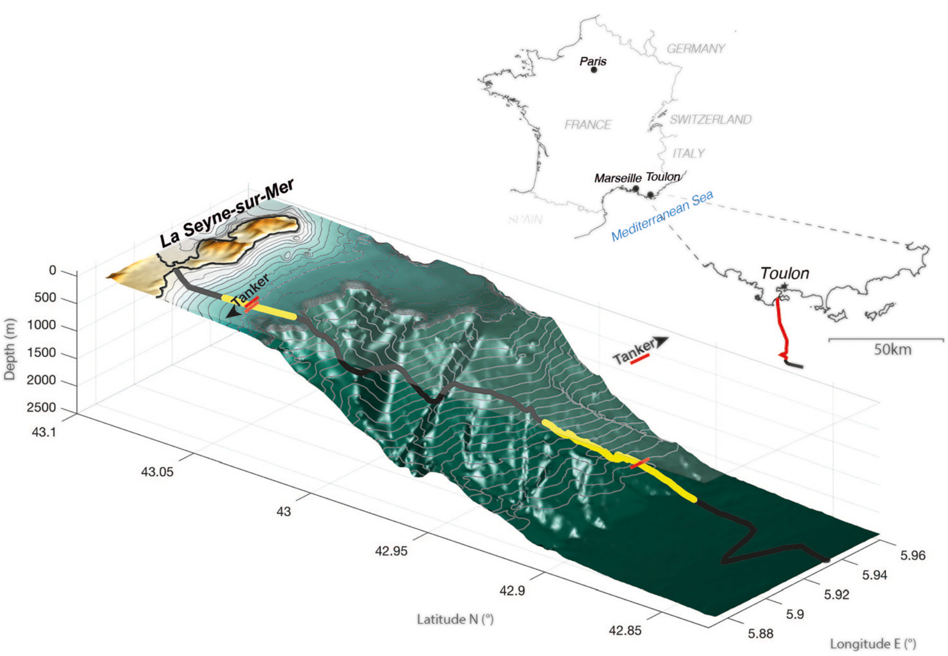

FIG. 2. (Color online) Location of the MEUST-Numerenv optical fiber offshore of La Seyne-sur-Mer located in the vicinity of Toulon, south of France. The 41.5 km cable lies on the continental shelf for the first 7.5 km before reaching the steep continental slope. The first 35 km of the cable is indicated by the red section of the cable indicated in the map. The first route of the tanker at 5.8 km from the coast and the second route at 20 km from the coast, known from the AIS GPS positions, are shown by the red thick line on the sea surface. The projection of the tanker routes crossing the cable at 5.8 and 20 km is indicated by the red lines on the sea floor. The two yellow sections of the cable indicate the portion of the fiber we used to detect the acoustic waves emitted by the ship.

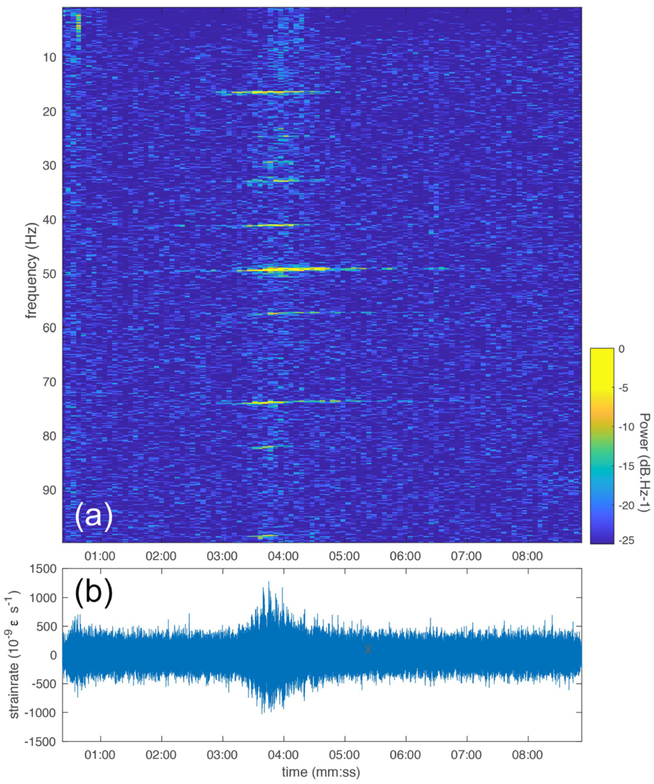

FIG. 3. (Color online) Analysis of the temporal and spectral radiated noise of the tanker when passing above the optical fiber section 5.8 km from the shore and 85 m deep. (a) Power spectrogram density of the recorded strain-rate measured on 10 s long windows with an overlap of 50% on the fiber at 5.651 km from the shore between 0 and 100 Hz and relative to the maximum power of $20 \times 10^{-6} \varepsilon^2 \, s^{-2}$ at the dominant frequency 49 Hz. (b) The corresponding time series.

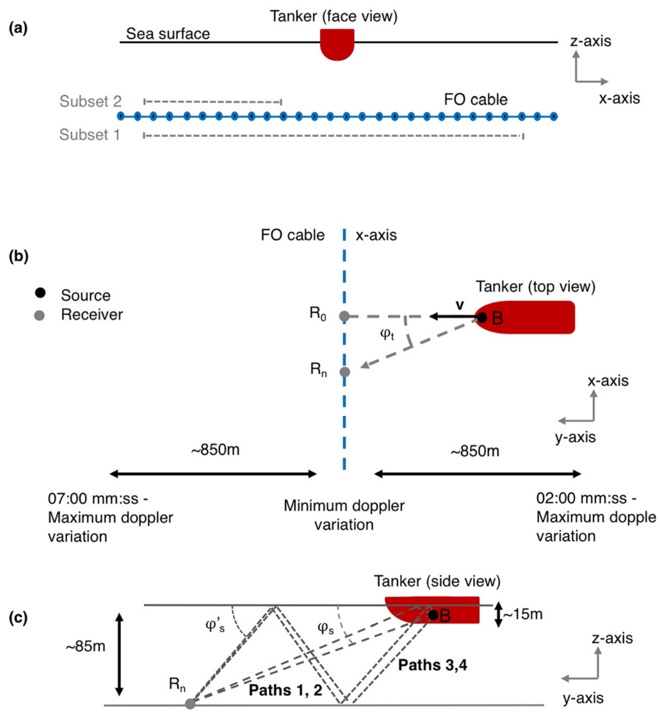

FIG. 4. (Color online) Ship displacement (a) face, (b) top, and (c) side views. The trajectory of the tanker B is described by the velocity vector **v**. R_0 is the closest receiver to the axis of the tanker, and R_n indicates another receiver on the fiber-optic (FO) cable. Ray paths are shown by dashed lines (assuming that ray approximation is valid, i.e., for high enough frequencies). Angles φ_t and φ_s are, respectively, the projections on the horizontal plane xBy and on the vertical plane yBz of the angle φ between the boat trajectory and the direct path from the boat to the receiver R_n.

maximum energy received from the passing boat. These narrowband signals, with high SNR, appear in the strain-rate time-frequency diagram, as the boat approaches the fiber [Fig. 3(a)]. At its dominant frequency, around 49 Hz, the power of the boat radiated noise, averaged over an interval of 9 min, is 18 dB/Hz higher than the environmental and instrumental noise [Fig. 3(a)]. Considering the mean ship velocity given by the AIS system during this period (about 11 knots) and its route (almost perpendicular to the fiber), it means that the 49 Hz signal from the ship is recorded over 1700 m. And if the boat displacement is roughly symmetric across the fiber, it means that the signal starts to be detected about 850 m away from the fiber (Fig. 4). On the strain-rate time series, the ship radiated noise level increases by a factor of 2 in a time window of 1 min [Fig. 3(b)].

At 2000 m depth, the acoustic noise emitted from the boat is more attenuated, and the SNR is lower (Fig. 5). Hardly any significant increase in the amplitude of strain-rate time series is observed when the tanker passes over the cable. Still, after time-spectral analysis, we identify narrow bands with high energy and some at the same frequency as those observed at shallow depth. At its dominant frequency, 49 Hz, the power of the spectral line reaches 8 dB/Hz higher than noise on average during the 9 min of records. Another line around 57 Hz is still visible. However, spectral lines around 16, 33, 41, 76, and 83 Hz observed on the first day at shallow depth are not visible. This can be caused by changes in the tanker speed, heterogeneous ground coupling along the cable, and the greater attenuation of the acoustic waves in the 2000 m water column. Besides, at higher depth, wave propagation can be affected by the velocity profile of the water column so that some rays can be refracted without reaching the bottom. Nevertheless, at short range, the propagation is mainly top-down, so that bottom reflection can occur even if the sub-surface velocity differs from the water velocity. Using a constant velocity gradient of $0.016\,m{\cdot}s^{-1}$ commonly used for the Mediterranean Sea below 200 m (e.g., Salon *et al.*, 2003), we found that the different paths that reach the bottom at 2000 m depth are almost straight up to 8 km away from a surface source. See the supplementary material[1] for the ray tracing model.

By computing short Fourier transforms every 4 s for each receiver in the vicinity of the ship, we monitor in space and time the power of spectral lines radiated by the ship as it travels above the fiber at 85 m (Fig. 6). We observe that the distance range at which we can detect the tanker changes as a function of the frequency. Both the signal power and the attenuation of acoustic waves depend on the frequency and therefore control the distance over which we detect a signal. Another important feature is ring-like high-power patterns, clearly visible at 41, 49, and 57 Hz, related to the

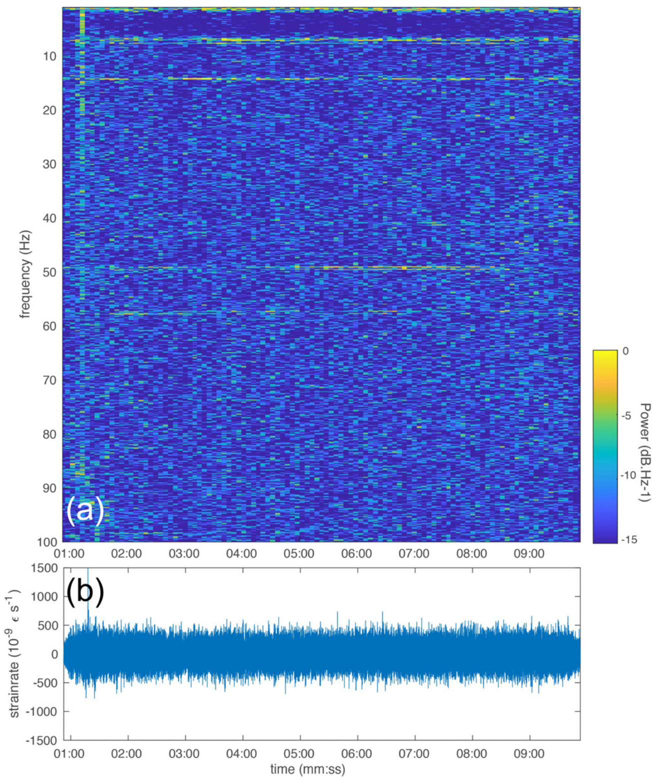

FIG. 5. (Color online) Analysis of the temporal and spectral radiated noise of the tanker when passing above the optical fiber section 20 km from the shore and 2000 m deep. (a) Power spectrogram of the recorded strain-rate measured on 10 s long windows with an overlap of 50% on the fiber at 19.494 km from the shore between 0 and 100 Hz relative to the maximum power of 6.7 $\times 10^{-6} \varepsilon^2$ s^{-2} at the dominant frequency 49 Hz. (b) The corresponding time series.

interference of acoustic waves reflected from the surface and the sea bottom (see Sec. IV). At 17 Hz, the ring-like pattern is not visible, probably because the wavelength at this frequency equals the water layer thickness and is controlled by a modal propagation. Using MOCTESUMA (a coupled normal-mode model) (Etter, 2012, 2018) and taking into account four layers in the bottom, we found that 17 modes can propagate with this frequency and at this channel depth.

We perform the same type of analysis for the tanker when it is cruising above a 2000 m deep section of the fiber-optic cable (Fig. 7). Because of the more complex bathymetry, it is harder to track the accurate position of the tanker from these maps. However, high power at different frequencies between 4 and 6 min and between 20 and 21 km indicates a position of the boat close to the fiber and consistent with AIS records.

IV. OPTICAL FIBER CABLE RESPONSE TO AN ACOUSTIC POINT SOURCE

We model the intensity of the wavefield in time and space for an acoustic point source using plane waves following ray trajectories. We convert the acoustic wave into the longitudinal strain-rate and compute the fiber-optic response for the specified gauge length.

We express the strain and strain-rate for acoustic waves reaching the fiber and sensed by DAS in an iso-speed water profile, following the same approach as proposed by Bakku (2015) for P-waves (Appendix A). For an incoming acoustic wave with particle velocity A_v, angular frequency ω, wavenumber $\vec{k}$, and propagation velocity c, the corresponding strain induced along the x axis of the fiber can be written as

$$\varepsilon_{xx} = \frac{-A_v}{c} \cos^2\theta e^{i(\omega t - \vec{k}\cdot\vec{r})}, \tag{1}$$

where θ is the angle between $\vec{k}$ and the x axis, $\vec{r}$ is the vector between the source and the receiver, ω is the pulsation, and t is the time. The DAS measures strain-rate averaged over the gauge length L, leading to the following response:

$$\dot{\varepsilon}_{DAS} = \dot{\varepsilon}_{xx} \mathrm{sinc}\left(k_x \frac{L}{2}\right). \tag{2}$$

This is equivalent to the difference in particle velocities on the x axis component of two geophones separated by L (Mateeva *et al.*, 2014).

Assuming the source is located at 15 m depth, taking into account the tanker draft, eight acoustic rays have been used to predict the radiated sound field (see Fig. 4). Adding more paths did not change the intensity maps. Path 1 runs from the source directly to each receiver. Path 2 has approximately the same path but hits the surface first. Both paths are represented by dashed lines in Fig. 4(b). Other paths are deduced by adding one, two, or more bottom-surface reflection sequences to paths 1 and 2. For example, paths 3 and 4 are represented in dashed lines in Fig. 4(b). The reflection coefficient depends on the incident angle—the Fresnel coefficient is computed and applied for each reflection—and on the nature of the soil, mainly composed by shales (Mascle, 1971) (Appendix B). In a 90 m depth water channel and using wavefield modal description, Turgut *et al.* (2010) showed interferences of acoustic waves reflected on the sea surface for a source located at a depth down to $\lambda/4$. With a source at 15 m, for frequencies higher than 25 Hz, such interferences should be measured on the seafloor.

The intensity maps have been simulated over 4 min of record for the two, four, and eight first paths at 49.4 Hz [Figs. 8(a)–8(c)]. Figure 4 shows paths 1–4. Paths 5–8 are the next multiples. In Fig. 8(a), we observe a symmetric shape with intensity reaching zero when k_x equals zero, due to the null response of the fiber in the direction perpendicular to the cable (broadside). The figure has only two lobes of high intensity, as we only model the direct path of the acoustic waves. In Fig. 8(b), which includes four paths, we observe a kind of ring shape that becomes more obvious in Fig. 8(c) with eight paths modeled. The comparison of Fig. 7(a) to Fig. 7(c) allows us to understand the origin of the ring shape we observe in the real data (Fig. 5). Due to the ship's motion over the fiber, the multipath interferences are

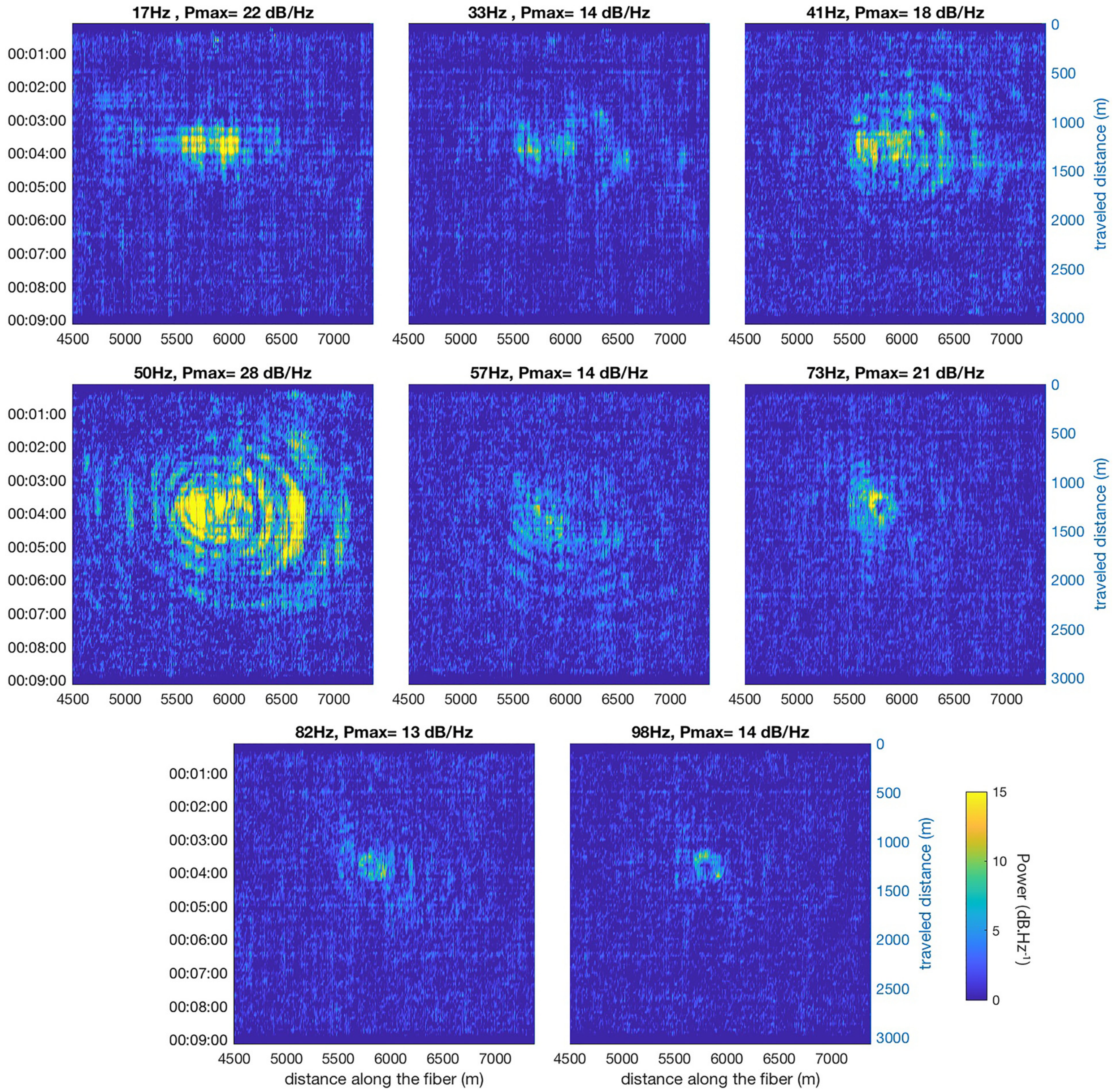

FIG. 6. (Color online) Acoustic noise power of the spectral lines radiated by the ship in space and time, on 10 s long windows with an overlap of 50%, when passing above a section of fiber-optic cable 85 m deep. The distance traveled by the boat and the time of the measurement are indicated on the right and left sides of the figures, respectively. The distance traveled by the boat is estimated from its velocity of 11 knots. On each figure, the title indicates the central frequency of the analysis in a 1 Hz narrow band as well as the maximum recorded power relative to instrumental and environmental noise measured at $191 \times 10^{-9} \varepsilon^2\,s^{-2}$ in the [17, 100] Hz frequency band. Note that the distance along the fiber is measured from the shore.

permanently varying and create ring shapes on the 49.4 Hz response.

The shape of the eight-path model prediction is not exactly the same as the one recorded on the fiber [Fig. 8(d)]. Many reasons can explain this discrepancy: varying coupling of the fiber, varying depth for the considered area, and possible fiber curvature. Besides, for the recorded data, we could not separate the two emitted frequencies close to 49.5 Hz in the intensity maps. Nevertheless, the size and spacing of the ring-like shapes are similar enough so that the signals recorded by the fiber appear to come from acoustic multipath interfering within the water channel. Underwater telecom cables, therefore, also behave as seismometers recording elastic signals coming from the ground (e.g., Sladen *et al.*, 2019) and pressure waves from inside the water layer.

In this section, we have illustrated the DAS capability of recording acoustic waves in an underwater environment at both shallow and intermediate depths. We have also demonstrated that it is possible to explain the seemingly complex signal patterns recorded by DAS by taking into account the acoustic wave reverberations and the specific broadside response of the fiber. We now explore the possibility to record and model the Doppler shift caused by the tanker motion.

https://doi.org/10.1121/10.0004129

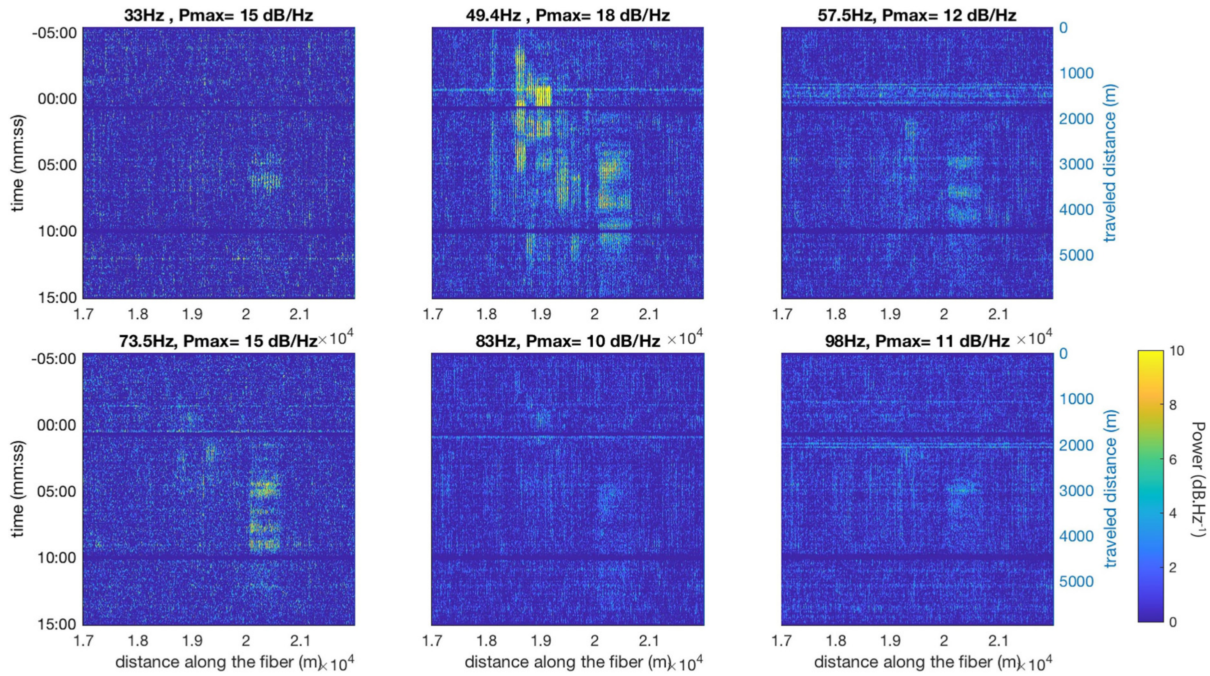

FIG. 7. (Color online) Acoustic noise power of the spectral lines radiated by the ship in space and time on 10 s long windows with an overlap of 50%, when passing above a section of fiber-optic cable 2000 m deep. The distance and time traveled by the boat are indicated on the right and left sides of the figures, respectively. The distance traveled by the boat is derived from its velocity of 7.8 knots. On each figure, the title indicates the central frequency of the analysis in a 1 Hz narrow band as well as the maximum recorded power and the maximum recorded power relative to instrumental and environmental noise measured at $206 \times 10^{-9} \varepsilon^2\,\mathrm{s}^{-2}$ in the [17, 100] Hz frequency band. Note that the distance along the fiber is measured from the shore.

V. DOPPLER ESTIMATION

Let us consider a single tonal at frequency f_0 radiated by a ship moving at constant velocity v. For a given receiver R_n, the angle between the boat trajectory and the vector going from the boat to R_n (direct path) is noted φ. This angle is described in three dimensions using Figs. 4(b) and 4(c). The instantaneous frequency of the signal received on a given receiver at time t is

$$f(t) = f_0 + \Delta f(t), \quad (3)$$

with

$$\Delta f = f_0 \cdot v \cdot \frac{\cos\varphi}{c}, \quad (4)$$

where c is the sound speed in the medium and v is the velocity of the tanker. Considering a boat moving in a direction perpendicular toward the fiber, as depicted in Fig. 4(c), φ is minimum when the boat is far away from the fiber, and the Doppler frequency shift is maximum. The Doppler frequency shift then decreases when the boat gets closer to the fiber and reaches a minimum value when the boat crosses the fiber. Finally, it increases while the boat travels away from the fiber.

In the case of multipathed rays, and assuming a relatively plane sea bottom, we consider reflections at the bottom and the surface. For multipath 3 and 4 [Fig. 4(c)], with one reflection at the bottom, we call φ' the angle between the boat trajectory and the vector going from the boat to a

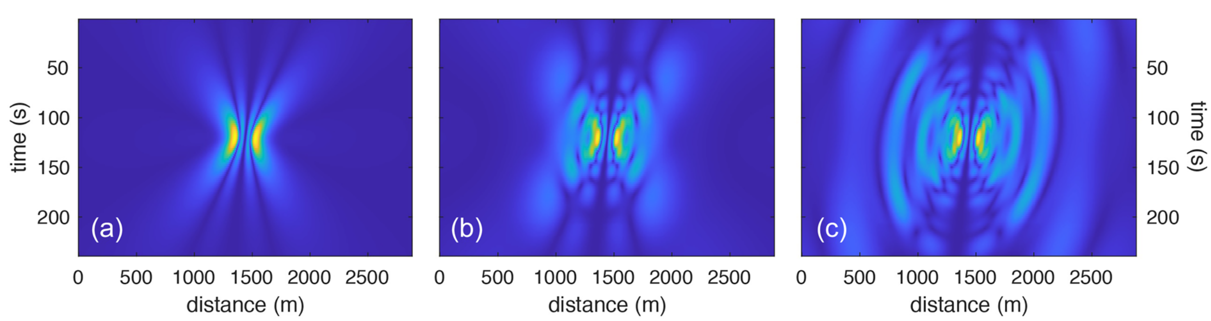

FIG. 8. (Color online) Simulated signal intensity recorded by a fiber-optic cable, 85 m deep, for a 49.4 Hz source at the surface moving almost perpendicular to the fiber (80° bearing) with a constant velocity of 11 knots. From left to right, the subset figures correspond to simulations acknowledging more reverberations: (a) two paths, (b) four paths, and (c) eight paths [see Fig. 4(b) for a schematic description]. Figures are created from simulations computed every 4 s. The received signal is computed at every time sample for a constant velocity of 1500 m/s in the water layer. The reflection coefficient for each ray takes into account the incidence angle and the nature of the seabed (shale). The model takes into account the fiber response—square cosine of the bearing—and geometrical spreading for amplitude.

given receiver R_n. We observe that φ' is closer to 90° than φ. If we consider multipathing with additional surface-bottom reflections, the angle φ' will always increase and get closer to 90°. As a consequence, when ray theory applies and for a relatively plane bottom, the maximum Doppler frequency shift will be reached for the direct path.

The usual way to estimate the Doppler shift is to use a time-frequency representation of the received signal at a given sensor. See supplementary material[1] for the time-frequency representation of 49 Hz spectral lines emitted by the boat when cruising above the cable at 85 and 2000 m water depth, respectively. While the estimation of the Doppler shift is straightforward, its accuracy depends on the trade-off between the resolution in time, controlled by the window's length, and the resolution in frequency, which is equal to the inverse of the window's length. Here, we prefer to analyze the signal through a *f-k* representation to take full advantage of the dense spatial distribution of the sensors. Because *f-k* decomposition is a global decomposition and the acoustic source is moving, the resulting spectral image will be blurred. Yet, even if the recorded signals are not coherent over the whole receiver subset, we see that the blurring effect is limited and that the *f-k* representation provides insightful details for interpretation.

Since we performed a *f-k* analysis on a subset of the DAS array centered on the plumb line of the boat when the boat crosses the fiber [subset 1 in Fig. 4(a)], the emitted signal is seen with positive and negative wavenumbers. We expect, on the one hand, a maximum shift of the Doppler frequency when the boat moves away from the fiber in a direction perpendicular to the fiber (i.e., a *k*-wavenumber close to zero on subset 1) and, on the other hand, a measured frequency close to the frequency emitted when the boat crosses the fiber, i.e., when the absolute wavenumber reaches its maximum at both ends of subset 1.

At 85 m depth, according to Sec. III, the ship starts to be detected around 49 Hz about 850 m away from the fiber. At this time and for the closest receiver on the fiber cable R_0 to the axis of the tanker [Fig. 4(b)], we can estimate φ using $\tan(\varphi) \approx 85/850 = 0.1$. This leads to an apparent velocity roughly equal to the tanker velocity for all the receivers in the vicinity of R_0. This also implies that the Doppler variation tends to its maximum possible value $\Delta f = f_0 \cdot v/c$. In the same way, when the 49 Hz record ends 5 min later, the distance of the fiber is about 850 m, and the Doppler variation tends to its maximum value but with opposite sign [Fig. 4(b)]. Between those two times, considering that the tanker velocity vector is approximatively perpendicular to the fiber, the tanker will cross the fiber with a minimum Doppler variation for the portion of the cable close to R_0.

Using two-dimensional (2D) fast Fourier transform (FFT) in time and space on the recorded DAS data, we represent 8 min-long strain-rate signal—including the 5 min 49 Hz detection described before—measured along 3 and 5 km of fiber in the *f-k* domain when the tanker was passing at 5.8 and 20 km offshore, respectively (Fig. 9). Note that the wavenumber k represented on the x axis has been divided by 2π so that $k = f/c$ instead of $k = \omega/c$. Then, for any point in the *f-k* domain, the slope is an estimation of the apparent velocity. When the boat is cruising close to the coast, we observe two ellipses of energy centered around 49.2 and 49.4 Hz for $k_x = 0$. These frequencies are shifted by the Doppler effect. Following the interpretation presented above, the two frequencies—49.2 and 49.4 Hz around the center of the ellipses—are the ones with minimum Doppler variations, i.e., two frequencies emitted by the tanker that can be recorded vertically above the fiber. For each ellipse, we measure a Doppler shift Δf of about 0.18 Hz from the center. Using Eq. (3), with $f_0 = 49.4$ Hz and $c = 1500$ m/s, it leads to a velocity of 5.5 m/s, which is very close to the 5.6 m/s

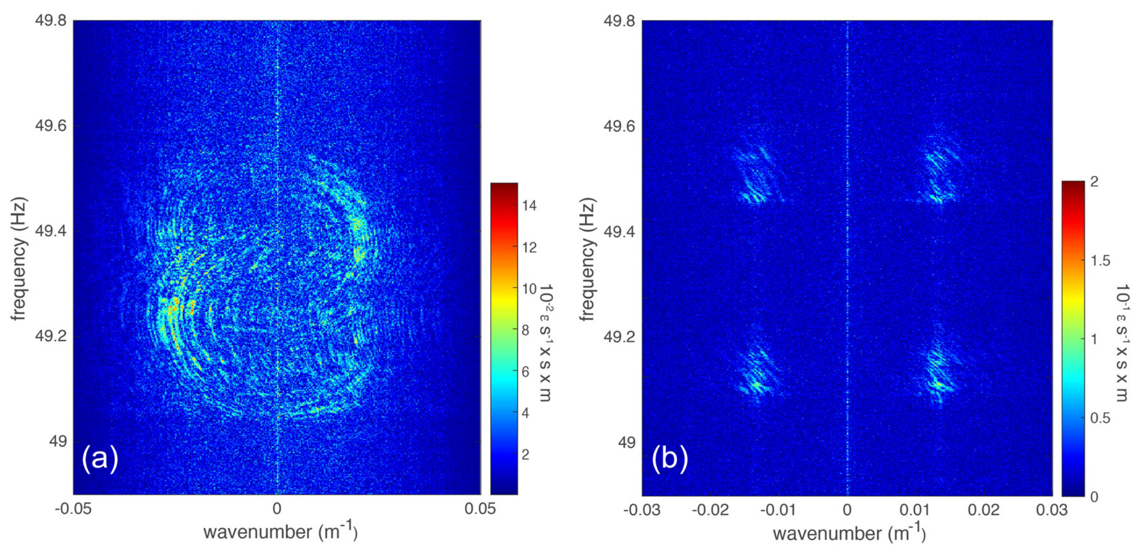

FIG. 9. (Color online) *f-k* decomposition of an 8 min long strain-rate signal recorded when the tanker is passing above (a) a shallow (85 m) section of the cable and (b) a deep section (2000 m). The signal is analyzed between 48.9 and 50.1 Hz and decomposed into seaward ($k_x < 0$) and landward ($k_x > 0$) propagating wavefield components. For the shallow section, the signal is averaged between km 4.5 and 7.5, and for the deep section, the signal is averaged between km 17 and 22 of the cable.

computed from AIS data. When shifted toward the higher or lower frequencies—the tanker traveling toward or away from the fiber—the wavenumber increases or decreases accordingly, assuming the wave velocity is constant.

At 2000 m depth (20 km offshore), the *f-k* processing shows higher energy at two different frequencies and on a narrow range of positive and negative wavenumbers. The two different frequencies are due to two distinct frequencies emitted by the boat around 49.5 Hz and are also responsible for the two ellipses observed at shallow depth [Fig. 9(a)]. Here, the Doppler shift is less pronounced, indicating a slower velocity of the tanker seen by the DAS [Fig. 9(b)]. On the abyssal plain, the geometrical spreading is larger; hence, a smaller portion of the cable senses the acoustic wave, and signals are detected for a small range of angles. Besides, for a given array, the section of the cable receiving signal close to 90° increases with depth, the source being further away. This is the reason why the range of wavenumbers excited is smaller for a boat cruising a deep sea and why null energy around $k = 0$ is more pronounced at greater depth.

The energy peaks around $k = \pm 0.015\,\mathrm{m}^{-1}$ come from sections of the cable that detect waves reaching the array with apparent velocity $c = c_0 \cos(\varphi) = f/k = 49.4/0.015 = 3293\,\mathrm{m/s}$, according to our convention for k. It therefore corresponds to an angle of 63°, i.e., about 900 m from the plumb line of the ship if ray curvature is neglected for this takeoff angle. Because the boat crosses the fiber with a nearly perpendicular route around the middle point of the selected portion of the fiber, the same energy is observed traveling landward (positive wavenumber) and seaward (negative wavenumber). The different coherent bands of energy with smaller frequency variations and smaller wavenumbers are related to acoustic waves reflected in the water column. To estimate the Doppler variation, we use a *f-k* representation of a 1.3 min-long strain-rate signal (Fig. 10). We estimate a maximum shift of 0.12 Hz at 49.05 Hz, corresponding to a velocity of 3.7 m/s—versus 4.0 m/s estimated from AIS positions.

To outline the main features of the *f-k* representation, we perform a simple modeling of the Doppler variation for a 49.4 Hz source traveling perpendicular to the cable at 5.65 m/s and measured on a 2880 m long cable section at 80 m and then at 2000 m depth. See the supplementary material[1] for the *f-k* representation of the synthetic signals. Although the model is simple, the main features of the observed *f-k* representation are visible on the modeled data: (1) the frequency at the center of the ellipse is equal to the emitted frequency and is the same for all paths, (2) the size of the ellipse decreases as the number of bottom reflections increases, and (3) at 2000 m depth, only signals with a wavenumber around $k = \pm 0.015\,\mathrm{m}^{-1}$ reach the fiber.

The *f-k* representation of underwater DAS records allows us to discriminate environmental signals efficiently from the instrumental noise of the DAS and acquisition system and could be used to detect acoustic signals in a systematic way. Properly modeling the acoustic propagation in the water column and the Doppler effect, taking into account the bathymetry and the fiber response, we find that it is possible to recover the position of the ship and its noise pattern both at shallow depth and in intermediate water depth.

VI. ASSESSING THE ABILITY TO RECOVER THE AZIMUTH FROM A KNOWN SOURCE

To detect and localize acoustic sources, arrays of sensors use various—and often multidimensional—algorithms, such as beamforming, with narrow- or wideband capabilities. DAS provides arrays of receivers that can be treated as an antenna, to accurately retrieve the azimuth of acoustic sources in the water column. In seismology, beamforming analysis of the DAS signal was successfully used (Lindsey *et al.*, 2017, 2019).

From a linear section of the fiber between 5613 and 5869 m, we track the bearing of the tanker using the tonal radiated in the 50 Hz frequency band. In theory, a longer array could be used. But, since the cable is not perfectly straight and due to a possible phase shift in the recorded data, we do not investigate longer arrays. We compare the bearing measured through beamforming with a simple synthetic case (Fig. 11). For DAS data, the beamforming is computed in the time domain every 5 s, and the center of the antenna is 59 m from the plumb line from the ship when

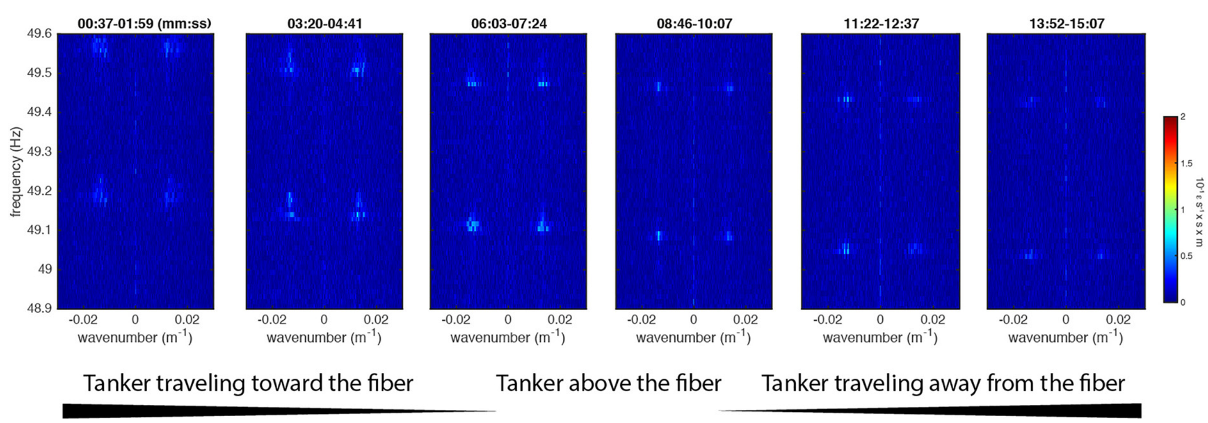

FIG. 10. (Color online) *f-k* decomposition of the strain-rate windowed on a 1.3 min long signal between 48.9 and 49.6 Hz, for seaward ($k < 0$) and landward ($k > 0$) components for the 17–22 km sections of the fiber when the tanker passed 2000 m above the cable.

https://doi.org/10.1121/10.0004129

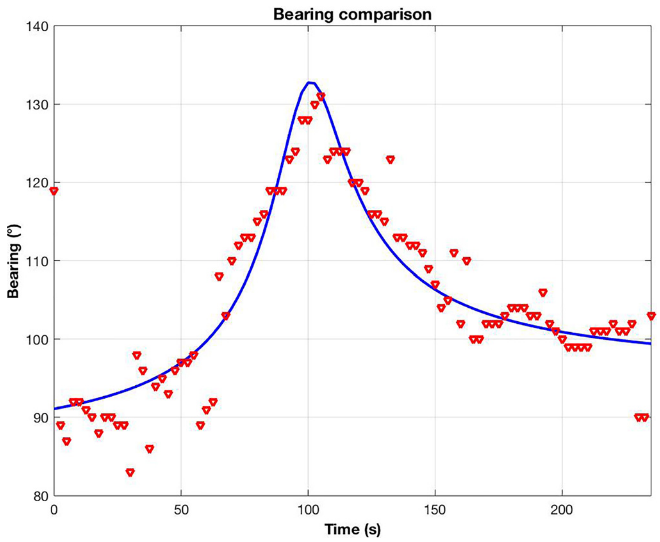

FIG. 11. (Color online) Bearing measurements performed using beamforming over a linear antenna of 256 m length and centered at 5741 m from the fiber extremity, i.e., 59 m away of the point where the ship crosses the fiber (red) compared with the theoretical bearing computed for a point 60 m away from the point where the ship crosses the fiber 65 m above the seafloor (blue). The beamforming is performed every 5 s using the recorded signal filtered in the [48, 51] Hz band.

crossing the fiber according to AIS data. Subset 2 in Fig. 4(a) indicates the position of the selected section of the fiber. In these conditions, the ship is seen at an approximately 90° bearing from the center of subset 2 when the ship is away from the fiber. The ship should deviate from this bearing until she crosses the fiber and then comes back to it as she moves away. At 50 Hz and for a 256 m long antenna, the angular resolution at 3 dB is 6°. For the synthetic case, we consider a ship crossing the x axis at an angle of 85° and a speed of 11 knots. With the channel at a depth of 80 m, we assume that the main source of noise radiated by the boat is 65 m above the seafloor. We compute the bearing angle of the ship from a point on the x axis 60 m away of the point where the ship crosses the x axis. In Fig. 11, we observe close agreement between the measured points (red triangles) and the simulated data (blue line). As expected, when the ship gets closer to the fiber, we observe a deviation from the initial bearing of 90°, between roughly 60 and 100 s before returning to it in a similar way.

Considering a water column of 85 m, we estimate that the boat crossed the fiber at a distance of 5821 m from the coast, whereas the real distance is closer to 5800 m according to the AIS positioning. This difference, which is about the width of the tanker, could be linked to depth approximation or AIS bias. In addition, the model used for the beamforming supposes a perfect alignment of the receiver, which is not proven. By reducing the array length to 128 m, the impact of a potential curvature of the fiber is reduced, and the newfound position becomes 5806 m instead of 5800 m.

VII. DISCUSSION

Our analysis demonstrates that it is possible to perform continuous and distributed monitoring of acoustic sources over several tens of kilometers using DAS and seafloor optical fiber cables. Acoustic waves traveling in the water layer interact directly with the fiber or penetrate the subsurface in case the cable is slightly buried in the sediments.

We detect and track a tanker in water up to 2000 m deep from the acoustic waves it produces. The appearance of frequency narrow bands in the time-frequency spectrum, over a given distance and at a given time, and a Doppler shift of the frequency with time are the characteristics of the noise emitted by a ship and are therefore quite easy to distinguish from environmental and DAS self-noise.

We model the principal features of the tanker acoustic signal using an analytical model. First-order features like the ring shape interference pattern and its energy decay right below the boat are well explained by the model, acknowledging reflections of the acoustic waves in the water column and the DAS broadside sensitivity. However, for more accurate modeling of the intensity of the acoustic field in time and space, numerical models taking into account the wavefront curvature, the full system response, the Doppler effect, the impedance of the sediments, and a non-constant water velocity profile should be used. Modeling of noise emitted by ships could also help to estimate the coupling of the cable with the ground, a critical step to calibrate the response of the cable and study non-anthropogenic signals—earthquakes, landslide, acoustic waves. More detailed analyses would probably require experiments with calibrated instruments, such as hydrophones. In addition, future DAS interrogator systems should provide access to higher frequencies and more complete monitoring.

Beamforming takes advantage of the distributed sensing capability of DAS to allow precise positioning of maritime vessels in both time and space. The example given in Sec. VI shows the impact of fiber positioning. Additional calibration (using, e.g., calibrated sources) could be used to better estimate the fiber response and position, which are a key points for providing sound pollution level measurements. Future beamforms should also integrate the azimuthal response of the fiber to improve the result of the beamforming algorithm. The acoustic noise of vessels cruising in deeper waters needs to be further explored. The attenuation of the acoustic wave with depth strongly depends on the celerity profile of the sea, and therefore could limit the range of depth in which we can detect signals with frequency higher than 100 Hz. Few existing fiber-optic cables can provide some insight about the feasibility to measure acoustic noise at depths greater than 2000 m because the repeaters limit the DAS sensing range to 30–50 km in general. However, on the first 30–50 km of cable, the depth is rarely greater than 2000 m, and it already offers a remarkable coverage.

We demonstrate the reliability of accurately measuring high-frequency signal (up to 100 Hz) on a telecom cable, which allows exploring other sources of acoustic signals in addition to seismic waves. The noise mapping that we presented confirms the multidisciplinary potential for DAS on seafloor cables.

VIII. CONCLUSION

We demonstrate the feasibility to record noise emitted by a boat at both shallow water (85 m) and in the deep sea (2000 m) using DAS on a standard underwater telecom cable, and we confirmed our inferences by comparison with AIS data. Using *f-k* representation, it is possible to discriminate between moving sources, static sources, and noise and to assess the speed of the moving sources by measuring the Doppler shift. Monitoring anthropogenic noise over a wide range of depths can help the scientific community to estimate its impact on marine life. Also, DAS telecom cables are very long underwater antennas (tens of kilometers) and very dense (every meter) and can serve to retrieve precisely the azimuth of noise sources, such as maritime vessels. If equipped with repeaters allowing the backscattered light to reach the DAS interrogator, worldwide telecom cables can serve as distributed environmental sensors measuring anthropogenic noise such as maritime traffic.

ACKNOWLEDGMENTS

This work was supported by the SEAFOOD project, funded in part by Grant No. ANR-17-CE04-0007 of the French Agence Nationale de la Recherche and in part by Université Côte d'Azur IDEX program Grant No. UCA JEDI ANR-15-IDEX-0001. We acknowledge the Centre de Physique des Particules de Marseille for facilitating access the infrastructure. The MEUST infrastructure is financed with the support of the CNRS/IN2P3, the Region Sud, France (CPER), the State (DRRT), and Europe (FEDER).

APPENDIX A: DAS SENSITIVITY TO INCIDENT ACOUSTIC WAVES ON THE FIBER-OPTIC CABLE

Acoustic waves that propagate in a 3D infinite homogeneous fluid medium are pressure fluctuations that can be modeled by the linear wave equation as described in Kinsler *et al.* (1999),

$$\nabla^2 p - \frac{1}{c^2}\frac{\partial^2 p}{\partial t} = 0, \tag{A1}$$

with p the acoustic pressure at a given position defined by the vector position $\vec{r} = (x, y, z)$, ∇^2 the Laplace operator, and c the acoustic wave velocity. We can express this acoustic wave in terms of a particle velocity $\boldsymbol{v}$ that is also governed by the linear wave equation

$$\nabla^2 \boldsymbol{v} - \frac{1}{c^2}\frac{\partial^2 \boldsymbol{v}}{\partial t} = 0. \tag{A2}$$

Considering a monochromatic plane wave traveling in a direction defined by the wave vector $\vec{k}$, the solution of Eq. (A2) is given by

$$v = A_v \hat{e}_k e^{i(\omega t - \vec{k}\cdot\vec{r})}, \tag{A3}$$

with ω the pulsation and $\hat{e}_k = \|\frac{\vec{k}}{k}\|$ the unit vector in the direction of propagation with k the wavenumber and A_v the amplitude of the planar wavefield of the particle velocity in the direction of propagation.

Taking the x axis of the coordinate system colinear to the fiber-optic cable, the wave vector $\vec{k}$ forms an angle θ with the x axis (also called the bearing angle). The projection of v along the x axis is

$$v_x = A_v \cos\theta e^{i(\omega t - \vec{k}\cdot\vec{r})}. \tag{A4}$$

The resulting strain ε_{xx}, which is a change in length Δl per unit of the original length l produced along the fiber, is given by

$$\varepsilon_{xx} = \frac{\partial u_x}{\partial x}. \tag{A5}$$

The particle velocity being the time derivative of the displacement, the displacement vector is given by $u_x = \frac{1}{i\omega} v_x$. We then express the strain as a function of the particle velocity,

$$\begin{aligned} &\varepsilon_{xx} = \frac{-k_x}{\omega} v_x, \quad \text{where } kx = k\cos\theta, \\ &\frac{-kA_v}{\omega}\cos^2\theta e^{i(\omega t - \vec{k}\cdot\vec{r})}, \quad c = \frac{\omega}{k}, \\ &\frac{-A_v}{c}\cos^2\theta e^{i(\omega t - \vec{k}\cdot\vec{r})}. \end{aligned} \tag{A6}$$

As shown in Eq. (A6), for acoustic waves, the measured strain along the x axis shows a square cosine dependence on the bearing angle. This dependence is the same for elastic P-waves (Mateeva *et al.*, 2014).

In DAS sensing, the strain along the fiber is measured over a gauge length L. The underlying principles of DAS sensing are reported in Masoudi and Newson (2016), Daley *et al.* (2016), and Jousset *et al.* (2018). Following Bakku (2015), the expression of ε_{xx}^{DAS} is given by

$$\begin{aligned} \varepsilon_{xx}^{DAS} &= \int_{z-\frac{L}{2}}^{z+\frac{L}{2}} \frac{\varepsilon_{xx}}{L} dx' \\ &= \frac{-A_v}{c}\cos^2\theta e^{i(\omega t - k_y y - k_z z)} \int_{z-\frac{L}{2}}^{z+\frac{L}{2}} e^{-ik_x x'} dx' \\ &\frac{A_v}{cL}\cos^2\theta \frac{e^{i(\omega t - k_y y - k_z z)}}{ik_x} [e^{-ik_x x'}]_{x-\frac{L}{2}}^{x+\frac{L}{2}} \\ &\frac{A_v}{cL}\cos^2\theta \frac{e^{i(\omega t - k_y y - k_z z)}}{ik_x} e^{-ik_x x}\left(-2i\sin\left(\frac{k_x L}{2}\right)\right) \\ &\frac{-A_v}{c}\cos^2\theta e^{i(\omega t - k_x x - k_y y - ik_z z)} \frac{\sin\left(\frac{k_x L}{2}\right)}{\frac{k_x L}{2}} \\ \varepsilon_{xx}^{DAS} &= \varepsilon_{xx}\operatorname{sinc}\left(\frac{k_x L}{2}\right). \end{aligned} \tag{A7}$$

Equation (A7) shows a sinc dependence on gauge length L of the strain measured using DAS. For a DAS that measures strain-rate, i.e., change in strain with respect to time, the sinc dependence still holds,

$$\dot{\varepsilon}_{xx}^{DAS} = \dot{\varepsilon}_{xx}\mathrm{sinc}\left(\frac{k_x L}{2}\right). \tag{A8}$$

APPENDIX B: MODELING OF ACOUSTIC SIGNALS MEASURED USING DAS

The synthetic data are simulated using ray theory. For each receiver at time t_r, the emitted time t_e and the distance traveled r are computed using a second order equation using a constant velocity. We neglect attenuation and assume that the amplitude is only influenced by geometrical spreading and possibly reflection coefficients. The DAS square cosine response is applied with regard to the bearing angle θ considering a fiber along the x axis, and the sinc dependence with gauge length L is added.

Then, for an emitted signal at frequency f_0, we get

$$u(t_r) = \frac{1}{r}\cos^2\theta\mathrm{sinc}\left(\frac{k_x L}{2}\right),$$

with $k_x = 2\pi f\cos\theta/c$.

In addition, for multipathed signals, two coefficients are added:

- -1.0 in the case of surface reflection,
- Fresnel coefficient $|Z_2\cos\theta_2 - Z_1\cos\theta_1/Z_2\cos\theta_2 + Z_1\cos\theta_1|$ in the case of bottom reflection, θ_1 and θ_2 being, respectively, the incidence angle and the transmitted angle and Z_1 and Z_2 the acoustic impedance of the water and of the first bottom layer. The impedance is equal to the density times the P-wave velocity $Z = \rho V_P$. For the bottom layer impedance, we used a V_P value of 4400 m/s and a density of 2500 $\mathrm{kg/m^3}$ for the shale (Mascle, 1971).

[1]See supplementary material at https://doi.org/10.1121/10.0004129 for the ray tracing model in a constant gradient $g = 0.01\ \mathrm{ms^{-1}}$ for a source located at 15 m depth and for the f-k representation of synthetic signal emitted by a moving source at 49.4 Hz traveling perpendicular to the cable.

Ajo-Franklin, J. B., Dou, S., Lindsey, N. J., Monga, I., Tracy, C., Robertson, M., Rodriguez-Tribaldos, V., Ulrich, C., Freifeld, B., Daley, T., and Li, X. (**2019**). "Distributed acoustic sensing using dark fiber for near-surface characterization and broadband seismic event detection," Sci. Rep. **9**, 1328.

Bakku, S. K. (**2015**). "Fracture characterization from seismic measurements in a borehole," Ph.D. dissertation, Massachusetts Institute of Technology, Cambridge, MA.

Coyle, P. (**2017**). "KM3NeT-ORCA: Oscillation research with cosmics in the abyss," J. Phys. Conf. Ser. **888**, 012024.

Daley, T. M., Freifeld, B. M., Ajo-Franklin, J., Dou, S., Pevzner, R., Shulakova, V., Kashikar, S., Miller, D. E., Goetz, J., Henninges, J., and Lueth, S. (**2013**). "Field testing of fiber-optic distributed acoustic sensing (DAS) for subsurface seismic monitoring," Leading Edge **32**, 699–942.

Daley, T., Miller, D. E., Dodds, K., Cook, P., and Freifield, B. M. (**2016**). "Field testing of modular borehole monitoring with simultaneous acoustic sensing and geophone vertical seismic profiles at Citronelle, Alabama," Geophys. Prospect. **64**, 1318–1334.

Dou, S., Lindsey, N. J., Wagner, A., Daley, T. M., Freifeld, B. M., Robertson, M., Peterson, J., Ulrich, C., Martin, E., and Ajo-Franklin, J. B. (**2017**). "Distributed acoustic sensing for seismic monitoring of the near surface: A traffic-noise interferometry case study," Sci. Rep. **7**(1), 11620.

Etter, P. C. (**2012**). "New frontiers for underwater acoustic modeling," *Proceedings of 2012 Oceans*, October 14–19, Hampton Roads, VA, pp. 1–10.

Etter, P. C. (**2018**). *Underwater Acoustic Modeling and Simulation*, 5th ed. (CRC, Boca Raton, FL).

Favali, P., and Beranzoli, L. (**2009**). "EMSO: European multidisciplinary seafloor observatory," Nucl. Instrum. Methods Phys. Res. Sect. A **602**(1), 21–27.

Feigl, K. L., and Parker, L. M. (**2019**). PoroTomo Final Technical Report: Poroelastic Tomography by Adjoint Inverse Modeling of Data from Seismology, Geodesy, and Hydrology (No. 3.1), University of Wisconsin, Madison, WI.

Fournier, G. (**2009**). "Hydroacoustique et bruit des navires" ("Hydroacoustics and vessel noise"), in Techniques de l'ingénieur. Bruit et vibrations, BR2030, https://www.techniques-ingenieur.fr/base-documentaire/ingenierie-des-transports-th14/hydrodynamique-navires-et-bateaux-42599210/hydroacoustique-et-bruit-des-navires-br2030/helices-br2030niv10004.html (Last viewed March 31, 2021).

Frisk, G. V. (**2012**). "Noiseonomics: The relationship between ambient noise levels in the sea and global economic trends," Sci. Rep. **2**, 437.

Gray, L. M., and Greeley, D. S. (**1980**). "Source level model for propeller blade rate radiation for the world's merchant fleet," J. Acoust. Soc. Am. **67**(2), 516–522.

Hello, Y., Royer, J. Y., Rivet, D., Charvis, P., Yegikyan, M., and Philippe, O. (**2019**). "New versatile autonomous platforms for long-term geophysical monitoring in the ocean," OCEANS 2019—Marseille, June 17–20, Marseille, France, pp. 1–8.

Hermannsen, L., Mikkelsen, L., Tougaard, J., Beedholm, K., Johnson, M., and Madsen, P. T. (**2019**). "Recreational vessels without Automatic Identification System (AIS) dominate anthropogenic noise contributions to a shallow water soundscape," Sci. Rep. **9**, 15477.

Hornman, J. C. (**2017**). "Field trial of seismic recording using distributed acoustic sensing with broadside sensitive fibre-optic cables," Geophys. Prospect. **65**(1), 35–46.

Jousset, P., Reinsch, T., Ryberg, T., Blanck, H., Clarke, A., Aghayev, R., Hersis, G. P., Henninges, J., Weber, M., and Krawczyk, C. M. (**2018**). "Dynamic strain determination using fiber-optic cables allows imaging of seismological and structural features," Nat. Commun. **9**, 2509.

Kinsler, L. E., Frey, A. R., Coppens, A. B., and Sanders, J. V. (**1999**). *Fundamentals of Acoustics*, 4th ed. (John Wiley and Sons, Hoboken, NJ).

Kuvshinov, B. N. (**2016**). "Interaction of helically wound fibre-optic cables with plane seismic waves," Geophys. Prospect. **64**(3), 671–688.

Lamare, P. (**2016**). "The MEUST deep sea infrastructure in the Toulon site," EPJ Web Conf. **116**, 09001.

Lellouch, A., Horne, S., Meadows, M. A., Farris, S., Nemeth, T., and Biondi, B. (**2019**). "DAS observations and modeling of perforation-induced guided waves in a shale reservoir," Leading Edge **38**(11), 858–864.

Lindsey, N. J., Dawe, T. C., and Ajo-Franklin, J. B. (**2019**). "Illuminating seafloor faults and ocean dynamics with dark fiber distributed acoustic sensing," Science **366**(6469), 1103–1107.

Lindsey, N. J., Martin, E. R., Dreger, D. S., Freifeld, B., Cole, S., James, S. R., Biondi, B. L., and Ajo-Franklin, J. B. (**2017**). "Fiber-optic network observations of earthquake wavefields," Geophys. Res. Lett. **44**, 11792–11799, https://doi.org/10.1002/2017GL075722.

Mascle, J. (**1971**). "Géologie sous-marine du canyon de Toulon," Cah. Océanogr. **23**, 241-250.

Masoudi, A., and Newson, T. P. (**2016**). "Contributed review: Distributed optical fibre dynamic strain sensing," Rev. Sci. Instrum. **87**, 011501.

Mateeva, A., Lopez, J., Mestayer, J., Wills, P., Cox, B., Kiyashchenko, D., Yang, Z., Berlang, W., Detomo, R., and Grandi, S. (**2013**). "Distributed acoustic sensing for reservoir monitoring with VSP," Leading Edge **32**, 1278–1283.

Mateeva, A., Lopez, J., Potters, H., Mestayer, J., Cox, B., Kiyashchenko, D., Wills, P., Grandi, S., Hornman, K., Kuvshinov, B., Berlang, W., Yang, Z., and Detomo, R. (**2014**). "Distributed acoustic sensing for reservoir monitoring with vertical seismic profiling," Geophys. Prospect. **62**(4), 679–692.

McKenna, M., Ross, D., Wiggins, S., and Hildebrand, J. (**2012**). "Underwater radiated noise from modern commercial ships," J. Acoust. Soc. Am. **131**(1), 92–103.

McKenna, M., Wiggins, S., and Hildebrand, J. (**2013**). "Relationship between container ship underwater noise levels and ship design, operational and oceanographic conditions," Sci. Rep. **3**, 1760.

Merchant, N. D. (**2019**). "Underwater noise abatement: Economic factors and policy options," Environ. Sci. Policy **92**, 116–123.

Miller, D. E., Daley, T. M., White, D., Freifeld, B. M., Robertson, M., Cocker, J., and Craven, M. (**2016**). "Simultaneous acquisition of distributed acoustic sensing VSP with multi-mode and single-mode fiber-optic cables and 3-component geophones at the Aquistore CO_2 storage site," CSEG Record **41**, 28–33.

Mustonen, M., Klauson, A., Folégot, T., and Clorennec, D. (**2020**). "Natural sound estimation in shallow water near shipping lane," J. Acoust. Soc. Am. **147**(2), EL177–EL183.

Nishimura, C. E., and Conlon, D. M. (**1994**). "IUSS dual use: Monitoring of whales and earthquakes using SOSUS," Mar. Technol. Soc. J. **27**(4), 13–21.

Pillon, D. (**2016**). "Introduction à la détection sous-marine passive" ("Introduction to passive underwater detection"), in Techniques de l'ingénieur, Bruit et vibrations (RAD6712), https://www.techniques-ingenieur.fr/base-documentaire/environnement-securite-th5/acoustique-des-transports-42523210/introduction-a-la-detection-sous-marine-passive-rad6712/ (Last viewed March 31, 2021).

Rønnekleiv, E., Brenne, J. K., Waagaard, O. H., and Moussakhani, B. (**2019**). "Distributed acoustic sensing for submarine cable protection," in *Proceedings of Suboptic2019*, April 8–11, New Orleans, LA.

Salon, S., Crise, A., Picco, P., de Marinis, E., and Gasparini, O. (**2003**). "Sound speed in the Mediterranean Sea: An analysis from a climatological data set," Ann. Geophys. **21**(3), 833–846.

Sladen, A., Rivet, D., Ampuero, J. P., De Barros, L., Hello, Y., Calbris, G., and Lamare, P. (**2019**). "Distributed sensing of earthquakes and ocean-solid Earth interactions on seafloor telecom cables," Nat. Commun. **10**(1), 5777.

Turgut, A., Orr, M., and Rouseff, D. (**2010**). "Broadband source localization using horizontal-beam acoustic intensity striations," J. Acoust. Soc. Am. **127**(1), 73–83.

Vespe, M., Visentini, I., Bryan, K., and Braca, P. (**2012**). "Unsupervised learning of maritime traffic patterns for anomaly detection," in *Proc*eedings of the *9th IET Data Fusion* & *Target Tracking Conf*erence: Algorithms & Applications, May 16 and 17, London.

Wales, S. C., and Heitmeyer, R. M. (**2002**). "An ensemble source spectra model for merchantship-radiated noise," J. Acoust. Soc. Am. **111**(3), 1211–1231.

Wales, S. C., and Heitmeyer, R. M. (**2011**). "Merchant ship-radiated noise source levels," J. Acoust. Soc. Am. **129**(4), 2366.

Wiggins, S. M., and Hildebrand, J. A. (**2007**). "High-frequency acoustic recording package (HARP) for broad-band, long-term marine mammal monitoring," *Proceedings of the International Symposium on Underwater Technology and Workshop on Scientific Use of Submarine Cables and Related Technologies*, April 17–20, Tokyo, pp. 551–557.

Williams, E. F., Fernández-Ruiz, M. R., Magalhaes, R., Vanthillo, R., Zhan, Z., González-Herráez, M., and Martins, H. F. (**2019**). "Distributed sensing of microseisms and teleseisms with submarine dark fibers," Nat. Commun. **10**, 5778.

Williams, R., Wright, A. J., Ashe, E., Blight, L. K., Bruintjes, R., Canessa, R., Clark, C. W., Cullis-Suzuki, S., Dakin, D. T., Erbe, C., Hammond, P. S., Merchant, N. D., O'Hara, P. D., Purser, J., Radford, A. N., Simpson, S. D., Thomas, L., and Wale, M. A. (**2015**). "Impacts of anthropogenic noise on marine life: Publication patterns, new discoveries, and future directions in research and management," Ocean Coast. Manag. **115**, 17–24.

Yu, C., Zhan, Z., Lindsey, N. J., Ajo-Franklin, J. B., and Robertson, M. (**2019**). "The potential of DAS in teleseismic studies: Insights from the Goldstone experiment," Geophys. Res. Lett. **46**(3), 1320–1328, https://doi.org/10.1029/2018GL081195.